REVIEW

Two-dimensional rate-independent plasticity using the element-based finite volume method

Paulo Vicente de Cassia Lima Pimenta[1] · Francisco Marcondes[1]

Abstract

The element-based finite volume method (EbFVM) is well established in computational fluid dynamics; in the last decade, it has been extended to several areas of engineering and physics interest, such as electromagnetism, acoustics, and structural mechanics analysis with complex geometrical shapes. This paper describes the treatment of the conservative EbFVM approach for two-dimensional isotropic elastic–plastic rate-independent problems. In particular, we use plane strain and plane stress approaches upon incremental thermal and mechanical loads. In order to verify the performance of the EbFVM, numerical results are compared with a commercial simulator. Finally, from the present implementation and the comparisons performed, we can ensure that EbFVM makes accurate prediction as the traditional numerical approach commonly employed for the solution of mechanics problems.

Keywords EbFVM · Mechanics expansion · Thermal expansion · Nonlinear material

1 Introduction

In general, equations describing continuous mechanics are successfully employed for the investigation of the physical behavior of solids and fluids. Unfortunately, except for simple problems, these equations do not have any analytical solution. However, the development of numerical approaches allows us to analyze, through approximate solutions, a large number of complex problems of engineering and physics.

Since the advent of digital computers, a wide number of discretization techniques have been proposed for the solution of several partial differential equations. However, the most popular numerical methods are finite element (FEM), finite difference (FDM), and finite volume (FVM) [1]. During this period, the FEM established itself as the standard approach in solid mechanics analysis [2, 3]. On the other hand, the FDM and the FVM have been established as very

efficient procedures in the computational fluid dynamics (CFD) [4–6]. In the last few decades, FEM has also been improved to model multi-physical problems, such as electromagnetism and fluid flow [1, 7]. The FVM and FDM have also been enhanced and nowadays have been successfully applied to a wide number of physical problems as well, for instance acoustics [8], solid–fluid iteration [9], and radiative heat transfer phenomenon [10]. A key issue that differentiates the FVM from FEM and FDM is the ability of the first aforementioned method to guarantee local conservation of the physical properties being evaluated [4–6, 11–13]. Such behavior is a desired property in any numerical method [5, 14, 15]; see, for instance, the hybrid finite element method [16–19].

The FVM is divided into two main approaches [1, 5], which are cell-centered [3, 15] and cell vertex [6, 20, 21]. The first procedure is an important variant of the FDM, where each element or cell of the grid is a control volume and the independent variable is evaluated at geometric center of each cell. This approach has been largely used in the context of structured grids, such as Cartesian [22], cylindrical [23], and boundary-fitted coordinates [24]. Despite the last type of grid being more suitable to represent complex geometries than the other grids mentioned, it still has drawbacks to model certain complex geometries [5]. This issue was overcome with the introduction of unstructured meshes;

✉ Francisco Marcondes
   marcondes@ufc.br

[1] Department of Metallurgical Engineering and Material Science, Federal University of Ceará, Campus do Pici, Bloco 729, Fortaleza, Ceará 60440-750, Brazil

see, for instance, [25]. The second procedure borrows from FEM the idea of elements and shape functions [1]. In cell vertex approach the control volume is constructed around each node of the grid (Fig. 1) [1, 5]. This methodology has advantages over the cell-centered approach, since it is well suitable for problems where the unknown has to be determined at the boundary of the domain [5] and it also can be easily implemented for both structured and unstructured grids. This method, in the context of the unstructured meshes, was initially called CVFEM (control volume-based finite element method) [1]. According to Maliska [4], the CVFVM nomination gives a wrong idea that we have finite element method based on control volumes. He replaced the original CVFEM terminology by EbFVM (element-based finite volume method), since we still have a conservative approach at the control volume level that borrows from finite element method the idea of elements and shape functions; see, for instance, [26]. From now on, this paper adopts this nomenclature.

The pioneer application of the EbFVM was devoted to analyzing the numericalsolution of Poisson's equation in the field of electromagnetism using triangular elements by Winslow [27]. Subsequently, the EbFVM was applied to heat transfer and fluid flow problems using triangular elements by Baliga and Patankar [13] and quadrilateral elements by Schneider and Zedan [28]. To the best of our knowledge, the first application of the EbFVM in computational solid mechanics (CSM) was performed by Fryer et al. [29] for solving elastic stress–strain equations. This was further followed by Bailey and Cross [30] for solving three-dimensional linear elastic problems. Later

Fig. 1 EbFVM discretization. Element, sub-control volumes, and control volumes

on, the EbFVM was extended to nonlinear CSM for two- and three-dimensional viscoplasticity by [5, 6], respectively, and by Fallah et al. [21] to analyze nonlinear geometrical problems. It is important to stress that EbFVM has received lot of attention in linear elastic CSM applications. On the other hand, just few works have addressed the use of EbFVM in nonlinear CSM area. Therefore, this work is considered to make an important contribution in this field.

Since the introduction of EbFVM to the CSM field, comparative discussions about performance and accuracy of the EbFVM over FEM within the CSM area were taken up. The pioneering investigative work was performed by Idelson and Oñate [31], and more recently by Vaz et al. [32] and Filippini et al. [14]. According to these authors, EbFVM is an accurate and stable approach for applications in CSM field. In this work, we apply the EbFVM to elastic–plastic rate-independent cases through the assumption of infinitesimal deformation using plane strain and plane stress under mechanical and thermal expansions. The numerical results are compared with the solution provided by the commercial simulator, ABAQUS, which uses Galerkin FEM.

2 Constitutive elastic–plastic relations

In this section, we present the general physical models which describe the behavior of elastic–plastic solids under small deformation.

2.1 Stress and deformation tensor relationship in the elastic domain

The stress tensor for an isotropic material can be expressed, in the context of linear elastic assumption, by means of the following equation:

$$d\sigma_{ij} = D^e_{ijkl} d\varepsilon^e_{kl}, \tag{1}$$

where $d\sigma_{ij}$ is known as the second-rank Cauchy stress increment tensor, D^e_{ijkl} is the fourth-rank isotropic elastic modulus tensor, and $d\varepsilon^e_{ij}$ is the second-rank elastic strain increment tensor. In terms of Lamé's constants, λ, and μ, the elastic modulus can be represented by

$$D^e_{ijkl} = \lambda \delta_{ij}\delta_{kl} + \mu\left(\delta_{ik}\delta_{jl} + \delta_{il}\delta_{jk}\right). \tag{2}$$

The Lamé's parameters are related to Young's modulus E and Poisson's ratio ν through the following expression:

$$\lambda = \frac{\nu E}{(1+\nu)(1-2\nu)} \text{ and } \mu = \frac{E}{2(1+\nu)}. \tag{3}$$

The basic relationship for the elastic strain is given by

$$d\varepsilon^e_{ij} = \left(\frac{\partial du_i}{\partial x_j} + \frac{\partial du_j}{\partial x_i}\right), \tag{4}$$
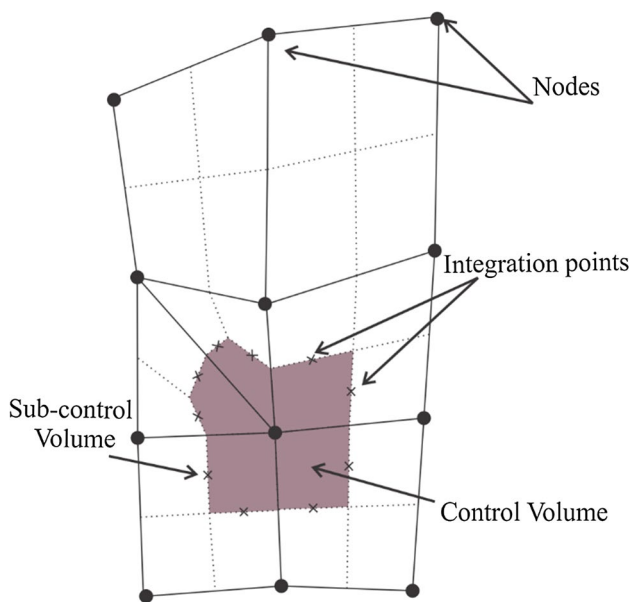
where du_i are the incremental displacement vector components.

When the variation in the temperature plays an important role in problems, which involve elasticity, the following thermal deformation tensor:

$$d\varepsilon_{ij}^{th} = \beta_{ij}\left(T - T_{\text{ref}}\right), \tag{5}$$

is added to Eq. (1), where β_{ij} is the thermal expansion tensor of the material, T is the local temperature, and T_{ref} is the reference temperature. From the assumption of isotropy, the thermal expansion tensor can be written as

$$\beta_{ij} = \alpha\delta_{ij}, \tag{6}$$

where α is thermal expansion coefficient.

Substituting Eqs. (2) and (5) into Eq. (1), we have the following relationship, in terms of Lamé's constants:

$$d\sigma_{ij} = 2\mu d\varepsilon_{ij} + \lambda d\varepsilon_{kk}\delta_{ij} - (2\mu + 3\lambda)\alpha(T - T_{\text{ref}})\delta_{ij}. \tag{7}$$

The above expression is known as Duhamel–Neumann formulation [33].

2.2 Strain tensor decomposition

The plasticity theory is able to characterize the mechanical behavior of materials beyond the boundaries of the elastic limit [34]. Basically, this theory can determine whether a given stress state falls within the elastic or plastic domain by means of the yield criterion function; in case of plasticity, it is able to perform corrections on the current stress state using the increment of plastic strain.

In this work, we assume the rate-independent plastic model through the assumption of the associative flow rule. Additionally, we shall work with the infinitesimal strain theory and von Mises yield criterion with isotropic hardening law. It is well known from the infinitesimal strain theory that the generalized increment of the total deformation $d\varepsilon_{ij}$ can be decomposed by the following expression:

$$d\varepsilon_{ij} = d\varepsilon_{ij}^e + d\varepsilon_{ij}^{th} + d\varepsilon_{ij}^p, \tag{8}$$

where $d\varepsilon_{ij}^p$ is the plastic strain increment. In the context of plasticity theory, the plastic strain increment for a general case can be written in terms of internal variables as [35]

$$d\varepsilon_{ij}^p = d\gamma\frac{\partial g}{\partial\sigma_{ij}} \tag{9}$$

where g is defined thermodynamically as the plastic potential function [34] and γ is a nonnegative plastic multiplier term [36].

2.3 Continuum plasticity relation for solid materials

If a material yields during a load, the mechanical behavior can no longer be described either by Eq. (1) or, in case of thermal load, by Eq. (7). The classical plasticity theory addresses this issue substituting the elastic deformation tension in Eqs. (1) by (8), i.e.,

$$d\sigma_{ij} = D_{ijkl}^e\left(d\varepsilon_{kl} - d\varepsilon_{kl}^{th} - d\varepsilon_{kl}^p\right). \tag{10}$$

The yield condition can be mathematically analyzed by means of the following expression:

$$f(\sigma_{ij}, \gamma) = \sqrt{3J_2(\sigma_{ij}^d)} - Y(\gamma), \tag{11}$$

where $J_2\left(J_2 = \frac{1}{2}\sigma_{ij}^d\sigma_{ij}^d\right)$ is second invariant of the stress deviator tensor 36, 37

$$\sigma_{ij}^d = \sigma_{ij} - \frac{1}{3}\delta_{ij}\sigma_{kk}, \tag{12}$$

and $Y(\gamma)$ is the uniaxial yield stress, which is experimentally determined. Here, we consider the associative flow rule, which means $f \equiv g$.

3 EbFVM approach

As discussed in Introduction, the EbFVM procedure borrows from FEM the idea of elements and shape functions. In particular, the shape functions are applied to interpolate the unknowns within each element of the grid. Take, for instance, the variable ϕ and the bilinear quadrilateral element (Fig. 1). Herein, we can evaluate the variable within each element using the following expression:

$$\phi \approx \sum_{i=1}^{4} N_i\phi_i. \tag{13}$$

The shape functions for the bilinear quadrilateral elements (Fig. 2) are given by [36]

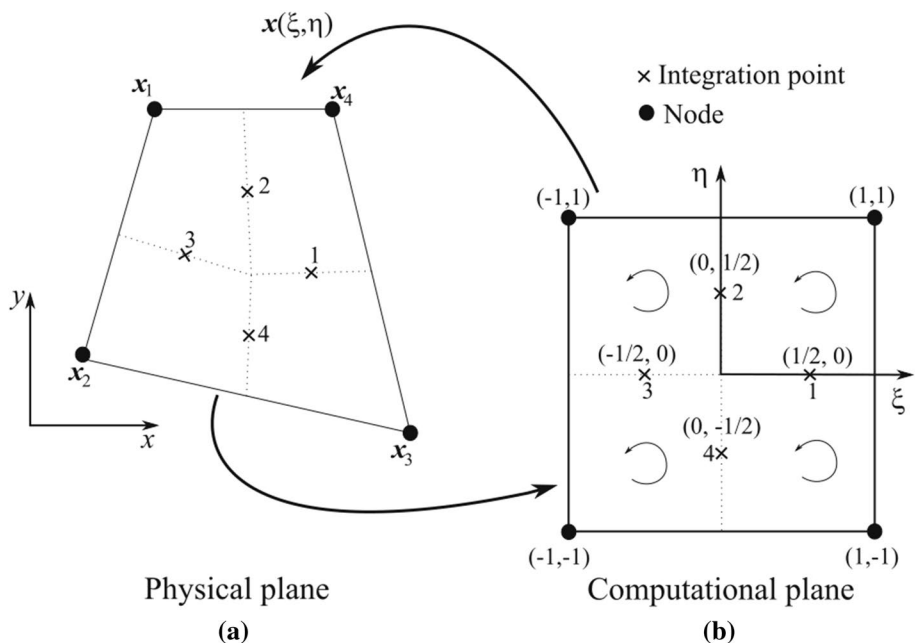$$N_1(\xi, \eta) = \frac{1}{4}(1 - \xi - \eta + \xi\eta), \tag{14}$$

$$N_2(\xi, \eta) = \frac{1}{4}(1 - \xi + \eta - \xi\eta), \tag{15}$$

$$N_3(\xi, \eta) = \frac{1}{4}(1 + \xi + \eta + \xi\eta), \tag{16}$$

$$N_4(\xi, \eta) = \frac{1}{4}(1 + \xi - \eta - \xi\eta), \tag{17}$$

and its derivatives are written as

Fig. 2 Bilinear quadrilateral element. **a** Physical plane and **b** computational plane

Physical plane
(a)

Computational plane
(b)

$$\frac{\partial N_i}{\partial x} = \frac{1}{|J|}\left(\frac{\partial y}{\partial \eta}\frac{\partial N_i}{\partial \xi} - \frac{\partial y}{\partial \xi}\frac{\partial N_i}{\partial \eta}\right), \tag{18}$$

$$\frac{\partial N_i}{\partial y} = \frac{1}{|J|}\left(\frac{\partial x}{\partial \xi}\frac{\partial N_i}{\partial \eta} - \frac{\partial x}{\partial \eta}\frac{\partial N_i}{\partial \xi}\right), \tag{19}$$

where $|J|$ is the Jacobian of the transformation, which is given by

$$|J| = \left(\frac{\partial x}{\partial \xi}\frac{\partial y}{\partial \eta} - \frac{\partial x}{\partial \eta}\frac{\partial y}{\partial \xi}\right). \tag{20}$$

The integration process that we present next occurs along the interface of each sub-control volume. The areas of each interface, in x- and y-directions, following a counterclockwise orientation are explicitly given by

$$n_x\Delta s = h\sum_{i=1}^{4}\left(\frac{\partial N_i}{\partial \xi}d\xi + \frac{\partial N_i}{\partial \eta}d\eta\right)y_i, \tag{21}$$

$$n_y\Delta s = -h\sum_{i=1}^{4}\left(\frac{\partial N_i}{\partial \xi}d\xi + \frac{\partial N_i}{\partial \eta}d\eta\right)x_i, \tag{22}$$

where h is the thickness of the domain.

3.1 Momentum conservation

We assume the integral of the simplified momentum equation for an arbitrary solid, with a volume V and boundary ∂S under

translation and rotation equilibrium [36]. Taking into account the above hypotheses, the momentum equation is given by

$$\oint_{\partial S} d\sigma_{ij}n_j ds = 0. \tag{23}$$

The force increments in Eq. (23) are suitable for three-dimensional stress analysis, which is given in Eq. (7). This general formula can be reduced for two-dimensional special cases, which are plane stress, plane strain, and axisymmetric (see details in [1, 7, 34, 36, 37]). For the purpose of this work, we rewrite Eq. (7) in a matrix form for plane stress and plane strain using Voigt notation [38]

$$\begin{bmatrix} d\sigma_{xx} \\ d\sigma_{yy} \\ d\sigma_{xy} \end{bmatrix} = \frac{E\bar{v}}{(1-v^2)}\begin{bmatrix} 1 & \zeta v & 0 \\ \zeta v & 1 & 0 \\ 0 & 0 & \frac{(1-v)}{2\bar{v}} \end{bmatrix}\left(\begin{bmatrix} d\varepsilon_{xx} \\ d\varepsilon_{yy} \\ 2d\varepsilon_{xy} \end{bmatrix} - \begin{bmatrix} 1 \\ 1 \\ 0 \end{bmatrix}\bar{\alpha}dT\right). \tag{24}$$

For convenience, the parameters ζ, $\bar{\alpha}$, and $\bar{v}$ are introduced in order to define plane stress ($\sigma_{zz} = \sigma_{zy} = \sigma_{zx} = 0$) and plane strain ($\varepsilon_{zz} = \varepsilon_{zy} = \varepsilon_{zx} = 0$). Additionally, for plane stress, we assume $\zeta = \bar{v} = 1$ and $\bar{\alpha} = \alpha$, and an additional term to evaluate the normal strain in z-direction

$$d\varepsilon_{zz} = -\frac{v}{E}(d\sigma_{xx} + d\sigma_{yy}) + \alpha dT. \tag{25}$$

We consider plane strain if $\zeta = \frac{1}{1-v}$, $\bar{\alpha} = (1+v)\alpha$, and $\bar{v} = \frac{(1-v)^2}{1-2v}$, with an additional term to evaluate the normal stress in z-direction

$$d\sigma_{zz} = -\frac{Ev(d\varepsilon_{xx} + d\varepsilon_{yy})}{(1-2v)(1+v)} + \frac{E\alpha dT}{1-2v}. \tag{26}$$

In the context of the Voigt notation, it is opportune to express the deformation tensor increment as a function of the displacement field as follows [38]:

$$\begin{bmatrix} d\varepsilon_{xx} \\ d\varepsilon_{yy} \\ 2d\varepsilon_{xy} \end{bmatrix} = \begin{bmatrix} \frac{\partial}{\partial x} & 0 \\ 0 & \frac{\partial}{\partial y} \\ \frac{\partial}{\partial y} & \frac{\partial}{\partial x} \end{bmatrix} \begin{bmatrix} du_x \\ du_y \end{bmatrix}, \tag{27}$$

or simply $[\varepsilon] = [L][du]$. Therefore, we are able to rewrite Eq. (27) by the following equation:

$$[d\sigma] = \left[D^e\right][L][du] - \left[D^e\right]I\bar{\alpha}dT, \tag{28}$$

where I represents the identity matrix expressed at the right-hand side in Eq. (28) using the Voigt notation.

Substituting Eqs. (28) into (23) and adjusting the notation, we obtain

$$\oint [n]\left[D^e\right][L][du] - [n]\left[D^e\right]I\bar{\alpha}dTds = 0, \tag{29}$$

where the unit normal vector n is defined as

$$n = \begin{bmatrix} n_x & 0 & n_y \\ 0 & n_y & n_x \end{bmatrix}. \tag{30}$$

Equation (35) is subtle for the treatment of elastic as well as for elastic–plastic problems. In the next section, we apply the EbFVM discretization in order to present a consistent approach to solve the nonlinear system of equations in elastic–plastic cases.

3.2 Boundary conditions

In order to achieve the solution of the physical model, appropriate boundary conditions have to be applied. They are defined by two sets: (I) ∂V_u, which specifies the prescribed displacement u_i^p and (II) ∂V_p, where the traction σ_{0i} is defined. In other terms, we have

$$u_i = u_i^p \quad \text{on } \partial S_u, \tag{31}$$

$$\sigma_{ij}n_j = \sigma_{0i} \quad \text{on } \partial S_p, \tag{32}$$

where n_j is the outward unit vector.

3.3 Integration procedure for the momentum equation

During the numerical integration, we have to ensure that the equilibrium condition, Eq. (23), must be satisfied in each incremental load, i.e.,

$$F_{\text{ext}} - F_{\text{int}} = 0, \tag{33}$$

where F_{ext} is the external force and F_{int} is the interval force vector.

In applications involving thermal variation, we assume that the temperature field does not affect the material properties. Additionally, in order to achieve quadratic convergence, we use a fully Newton–Raphson scheme. In this methodology, the tangent modulus, in the left-hand size of Eq. (23), must change in order to accommodate the new mechanical parameters when the material yields. Therefore, we rewrite Eq. (23) as

$$\oint [n]\left[D^{ep}\right][L][du] - [n]\left[D^e\right]I\bar{\alpha}dTds = F_{\text{ext}} - F_{\text{int}}(du), \tag{34}$$

where $D^{ep} = D^e$ for elastic loading and $D^{ep} = \frac{\partial \sigma}{\partial \varepsilon}$ for plastic loading; if the material yields during the process, D^{ep} is evaluated during the correction of the stress state in a process called *return mapping* [35–37]. This approach is discussed in Sect. 4.2.

The EbFVM approach integrates the constitutive equations in each sub-control volume (scv) of each element. Then, the global equations are assembled by using all scv that share the same node i. Assuming the notation in [6], we can rewrite Eq. (34) as

$$A_{ij}\Delta u_j = F_{i,\text{th}} + F_{i,\text{ext}} - F_{i,\text{int}}(\Delta u), \tag{35}$$

where

$$A_{ij} = \oint_{\partial S_i} [n]_i\left[D^e\right]\left[LN_j\right]ds, \tag{36}$$

where A_{ij} is the so-called global stiffness matrix [6, 14] and $F_{i,\text{th}}$ is the thermal force, which can be written as $F_{i,\text{th}} = B_i\Delta T_i$. Notice that the term $B_i = 0$ when there is no thermal effect; otherwise, it is evaluated by

$$B_i = \oint_{\partial S_i} [n]_i\left[D^e\right]I\bar{\alpha}\left[N_i\right]ds, \tag{37}$$

when the thermal variation is present. The external force is calculated as

$$F_{i,\text{ext}}^{n+1} = \oint_{\partial S_p} \sigma_{0i}ds. \tag{38}$$

4 Nonlinear numerical procedure

We present the Newton–Raphson procedure applied to non-equilibrium equation at the structural level (or global level), as well as to perform corrections over the stress state at the material level (integration points).

4.1 Non-equilibrium at the nodal level

When a plastic load increment takes place, the equilibrium relationship, Eq. (35), is nonlinear. Therefore, assuming a state of non-equilibrium for an initial estimate displacement u_i^n, we can rewrite Eq. (35) in a residual form introducing the iterative term δu as

$$A_{ij}\delta u_j^n = F_{i,\text{th}}^{n+1} + F_{i,\text{ext}}^{n+1} - F_{i,\text{int}}^n = R_i^n. \tag{39}$$

The Newton–Raphson approach is commonly used to linearize nonlinear equations, and at the same time, it provides a fast convergence rate, since it has quadric convergence near the root. During the iterative process, we ensure that the equilibrium condition is achieved using

$$\delta u_i^n = -\left[\frac{\partial R_i}{\partial u_j}\right]^{-1} R_j^n, \tag{40}$$

where $\left[\frac{\partial R_i}{\partial u_j}\right] \equiv A_{ij}$.

The displacement is updated using the following approximation:

$$u_i^{n+1} = u_i^n + \delta u_i^n, \tag{41}$$

and the increment Δu_i^{n+1} is evaluated using the last converged displacement calculated in the previous increment of force u_i^*

$$\Delta u_i^{n+1} = u_i^{n+1} - u_i^*. \tag{42}$$

The next step is to visit each element and calculate the stress increment at each integration point k using Eq. (28), which is written in an incremental format as

$$\Delta \sigma_k^{n+1} = \sum_{i=1}^{4} \left[D^e\right]\left[LN_i\right]_k\left[\Delta u_i^{n+1}\right] - \left[D^e\right]I\bar{\alpha}\left[N_i\right]_k\Delta T_i, \tag{43}$$

and the new stress tensor is updated, in each integration point k, in terms of the previous converged stress state σ_k^*

$$\sigma_k^{n+1} = \sigma_k^* + \Delta\sigma_k^{n+1}. \tag{44}$$

With the stress field given by Eq. (44) and using Eq. (11), we are able to observe if the nature of the stress state is elastic or plastic in each integration point of each element. As mentioned in Sect. 2.3, if $f < 0$, the stress state is elastic. Therefore, Eq. (44) represents the current stress field and $D^{ep} = D^e$, i.e., no corrections are necessary for this case. Otherwise, if $f \geq 0$, we must correct the stress state, as well as calculate the tangent modulus D^{ep} ($D^{ep} = \frac{\partial\sigma}{\partial\varepsilon}$). The approach responsible for this process is presented in the next section (Sect. 4.2), and it is called *return mapping*.

The next step, in the nonlinear solution process, is to calculate the internal force vector at the nodes. If no yields in strength take place, the stress obtained with Eq. (44) is

going to be used; on the other hand, if the material yields, the stress tensor is evaluated with the stress field provided by the return mapping. Therefore, independent of whether the stress state is elastic or plastic, the new internal force must be calculated by integrating the stress tensor evaluated at each integration point *k of each sub-control volume of each element that share the ith node*. The following expression is applied in order to calculate the internal force:

$$F_{i,\text{int}}^{n+1}(\Delta u_i^{n+1}) = \sum_{l=1}^{\text{nsvc}} \int_{\partial S} \sigma_k^{n+1}n\,\mathrm{d}s. \tag{45}$$

With this information, the new residual vector is given by

$$R_i^{n+1}(\Delta u_i^{n+1}) = F_{i,\text{th}}^{n+1} + F_{i,\text{ext}}^{n+1} - F_{i,\text{int}}^{n+1}(\Delta u_i^{n+1}). \tag{46}$$

In Eq. (45), nscv denotes the number of sub-control volumes that share the *ith* node of the grid. The iteration process stops if a given convergence criterion is satisfied. We adopted the L^2 norm of the ratio of the residual R and external force vector F_{ext} as a convergence criterion

$$\frac{\|R\|}{\|F_{\text{ext}}\|} < \epsilon, \tag{47}$$

where ϵ is the tolerance. In this work, ϵ is set to 10^{-10} for all case studies investigated.

The flowchart of the incremental procedure for the solution of the non-equilibrium momentum equations is shown in Fig. 3. This methodology requests the update of the stiffness matrix, at each integration point of the element, at each force increment, when yield occurs.
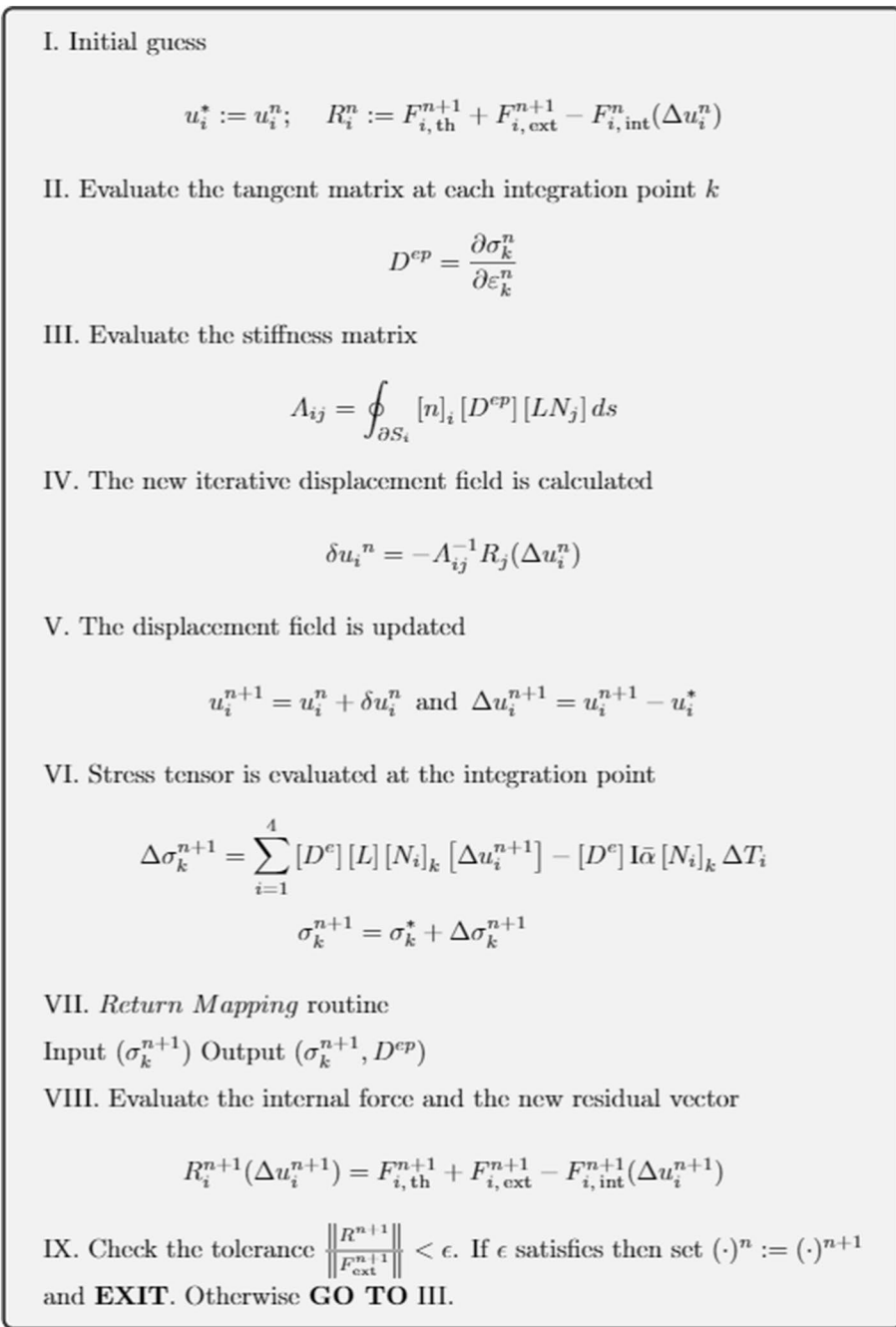
4.2 Implicit numerical integration of the return mapping

The classical rate-independent plastic model with isotropic von Mises hardening criterion is adopted in this work. For the treatment of the nonlinear equations involved in this theory, we assume an implicit integration on time, which is linearized with the Newton–Raphson method. The reasons for that choice lie on stability and quadratic convergence rate near the root. Thus, in case of plasticity, this numerical approach is used to correct the stress field when required in terms of the plastic parameters. This process is well known as return mapping.

It is important to mention that the integration performed in this section works for 2D and 3D domains without any restriction with exception for plane stress, since we also need to ensure that the component σ_{zz} is equal to zero. The implementation performed in this work for plane stress is based on [34].

The stress field calculated in Eq. (44) is adopted as the candidate stress tensor σ_k^c. Once the yield condition is

Fig. 3 Flowchart for the incremental procedure

I. Initial guess

$$u_i^* := u_i^n; \quad R_i^n := F_{i,\text{th}}^{n+1} + F_{i,\text{ext}}^{n+1} - F_{i,\text{int}}^n(\Delta u_i^n)$$

II. Evaluate the tangent matrix at each integration point k

$$D^{ep} = \frac{\partial \sigma_k^n}{\partial \varepsilon_k^n}$$

III. Evaluate the stiffness matrix

$$\Lambda_{ij} = \oint_{\partial S_i} [n]_i [D^{ep}] [LN_j] \, ds$$

IV. The new iterative displacement field is calculated

$$\delta u_i^n = -\Lambda_{ij}^{-1} R_j(\Delta u_i^n)$$

V. The displacement field is updated

$$u_i^{n+1} = u_i^n + \delta u_i^n \text{ and } \Delta u_i^{n+1} = u_i^{n+1} - u_i^*$$

VI. Stress tensor is evaluated at the integration point

$$\Delta \sigma_k^{n+1} = \sum_{i=1}^{4} [D^e][L][N_i]_k [\Delta u_i^{n+1}] - [D^e] I \bar{\alpha} [N_i]_k \Delta T_i$$

$$\sigma_k^{n+1} = \sigma_k^* + \Delta \sigma_k^{n+1}$$

VII. *Return Mapping* routine
Input (σ_k^{n+1}) Output (σ_k^{n+1}, D^{ep})
VIII. Evaluate the internal force and the new residual vector

$$R_i^{n+1}(\Delta u_i^{n+1}) = F_{i,\text{th}}^{n+1} + F_{i,\text{ext}}^{n+1} - F_{i,\text{int}}^{n+1}(\Delta u_i^{n+1})$$

IX. Check the tolerance $\left\| \frac{R^{n+1}}{F_{\text{ext}}^{n+1}} \right\| < \epsilon$. If ϵ satisfies then set $(\cdot)^n := (\cdot)^{n+1}$
and EXIT. Otherwise GO TO III.

verified, i.e., Equation (11) gives $f \geq 0$, the stress state is numerically corrected assuming the incremental form of Eq. (10), which is expressed using the definition of the deviator tensor (12), as well as the candidate stress state as [37]

$$\sigma_k^{n+1} = \sigma_k^c - D^e \Delta \gamma_k \sqrt{\frac{3}{2}} \frac{\sigma^d(\sigma_k^{n+1})}{||\sigma^d(\sigma_k^{n+1})||}, \tag{48}$$

where $\sigma_k^c = \sigma_k^* + \Delta \sigma_k^{n+1}$.

In order to differentiate the return mapping equations, we replace the superscript $n+1$ per j hereafter, since $n+1$ denotes the property in the structural iteration and j denotes the local iteration at the return mapping. We also rewrite Eqs. (48) and (11) in a residual form

$$[D^e]^{-1}\left(\sigma_k^j - \sigma_k^c\right) + \Delta \gamma_k^j \sqrt{\frac{3}{2}} \frac{\sigma^d(\sigma_k^j)}{||\sigma^d(\sigma_k^j)||} = R_\sigma^j, \tag{49}$$

$$\sqrt{3J_2\left(\sigma_k^j\right)} - Y(\Delta \gamma_k^j) = R_\gamma^j. \tag{50}$$

Applying the Newton–Raphson method to Eqs. (49) and (50) results in

$$\begin{bmatrix} \delta\sigma_k^{j+1} \\ \delta\gamma_k^{j+1} \end{bmatrix} = -[J]^{-1} \begin{bmatrix} R_\sigma^j \\ R_\gamma^j \end{bmatrix}, \tag{51}$$

where J is the Jacobian matrix given by

$$J = \begin{bmatrix} \frac{\partial R_\sigma}{\partial\sigma} & \frac{\partial R_\sigma}{\partial\gamma} \\ \frac{\partial R_\gamma}{\partial\sigma} & \frac{\partial R_\gamma}{\partial\gamma} \end{bmatrix}. \tag{52}$$

The new stress state and the new plastic parameter are updated as follows:

$$\sigma_k^{j+1} = \sigma_k^j + \delta\sigma_k^{j+1}, \tag{53}$$

$$\gamma_k^{j+1} = \gamma_k^j + \delta\gamma_k^{j+1}. \tag{54}$$

The above parameters are used to update the residue vectors R_σ^{j+1} and R_γ^{j+1}.

When the numerical iterative processes reach the convergence criterion, we are able to evaluate the tangent modulus $\left(D^{ep} = \frac{\partial\sigma_k^{j+1}}{\partial\epsilon_k^{j+1}}\right)$ using the following expression:

$$\begin{bmatrix} \partial\sigma_k^{j+1} \\ \delta\gamma_k^{j+1} \end{bmatrix} = \begin{bmatrix} D_{11} & D_{12} \\ D_{21} & D_{22} \end{bmatrix} \begin{bmatrix} \partial\epsilon_k^{j+1} \\ 0 \end{bmatrix}, \tag{55}$$

where $\partial\sigma_k^{j+1} = D_{11}\partial\epsilon_k^{j+1}$. This result leads to $D^{ep} = D_{11}$, which is the new tangent matrix at the integration point. The *return mapping algorithm* is shown in Fig. 4.

5 Nonlinear numerical procedure

In this section, we present four case studies to show the performance of the EbFVM for computational solid mechanics with nonlinearity material. These test cases are divided into two parts: (1) mechanical expansion and (2) thermal expansion, and for each one, we choose different domains, i.e., for the mechanical expansion we used the domain illustrated Fig. 5a and for the thermal expansion case we used the domain described in Fig. 5b.

The mechanical properties of the aluminum, required to define the elastic modulus are given by Young's modulus $E = 70$ GPa and Poisson's ratio $\nu = 0.2$. For the thermal expansion case study, in addition to the two aforementioned parameters, we also defined the thermal expansion coefficient $\alpha = 2.1 \times 10^{-5}$. The yield function for the linear plasticity relation was chosen as

$$Y(\gamma) = \sigma_Y + H'\gamma, \tag{56}$$

where σ_Y is the yield stress, which is given by $\sigma_Y = 0.243$ GPa. The angular coefficient was expressed by $H' = 0.2$ GPa and is equal to zero for the case of perfect plasticity.

We compare the numerical results with a reference solution in order to capture the accuracy of both EbFVM and FEM approaches. The reference solution was obtained by assuming a fine grid for both EbFVM and FEM approaches, where the results are expected to be grid independent.

5.1 Mechanical expansion

In this section we carry out numerical tests using a domain that corresponds to a plate with a hole at its center. This plate is stretched at its minimum section in the opposite directions, as shown in Fig. 5a. We analyze this numerical experiment from the point of view of perfect and linear plastic loads for plane strain and plane stress. For symmetry reasons, only one quarter of plate is investigated, i.e., the gray region depicted in Fig. 5a.

The boundary conditions are given by prescribed displacements, at the symmetry lines, and uniform surface tension $\sigma_{0i} = 0.1$ MPa, at the minimum section. The prescribed displacements are fixed in order to avoid rotation and translation of the domain.

For all simulations, the total load (0.1 MPa) is divided into 10 increments and the tolerance of $\epsilon = 10^{-10}$ is applied to check the global and local levels (Figs. 3 and 4). We use the last increment to present the profile of the equivalent stress along the minimum section of the plate. This region was chosen since it contains the concentration of the highest values of the stress state.
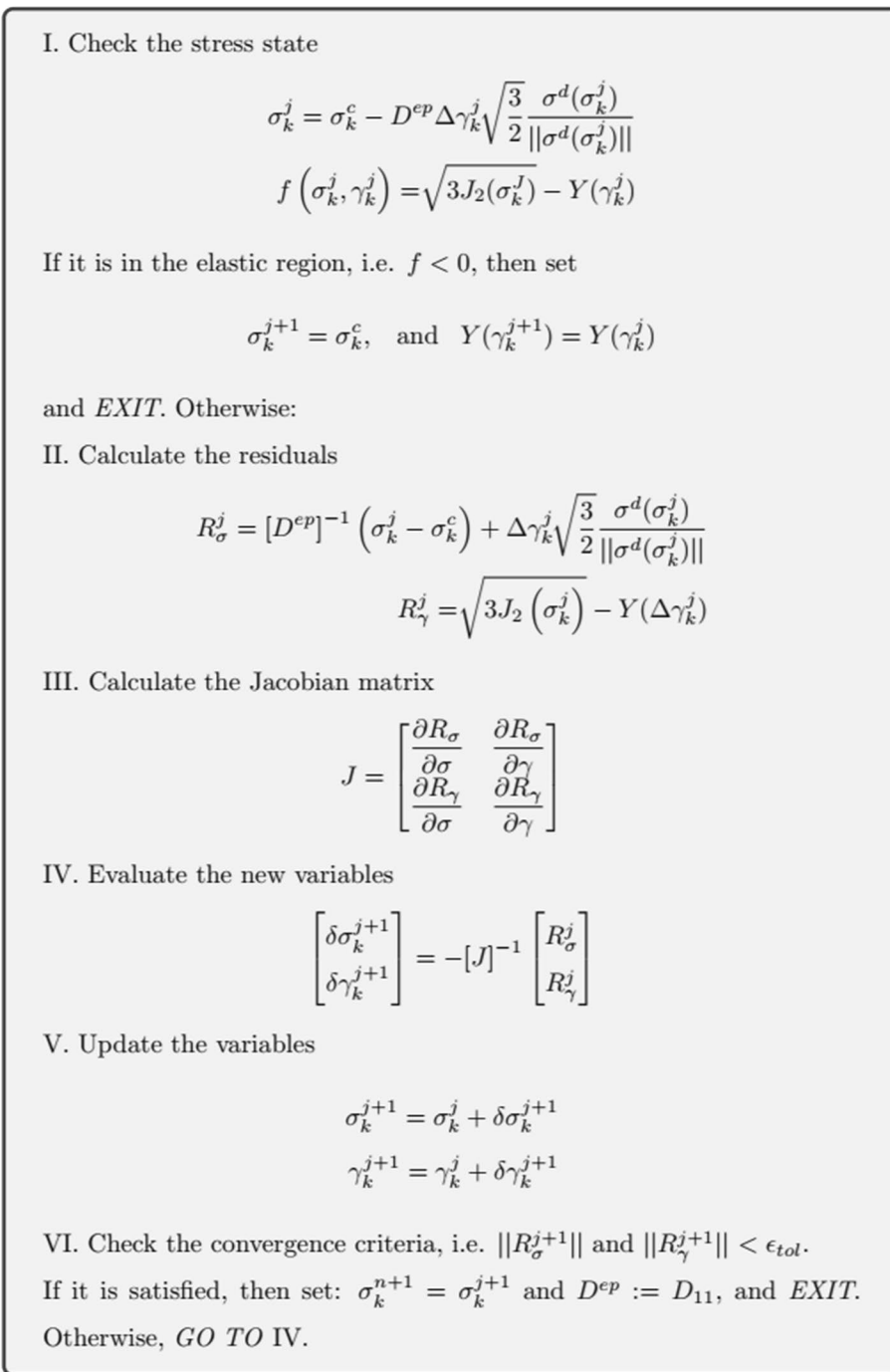
We analyze the convergence rate of the solution with the mesh size for both the EbFVM and FEM (via commercial simulator). In order to make a fair comparison between the two numerical approaches, we imported the mesh used in the ABAQUS simulator and applied our in-house simulator. The reference solution is assumed to be the numerical result obtained with the mesh with 7000 elements and 7697 nodes. Additionally, in the EbFVM context, we analyze the Newton–Raphson convergence rate at the global level, using the last time load step, for the smallest size mesh employed.

Figure 6a, b presents the errorreduction in EbFVM and FEM, respectively, as the mesh is refined under the plane strain and perfect plasticity assumption.

From Fig. 6a, b, it can be noticed that the numerical experiments using EbFVM were able to reach convergence rates equivalent to the ones using FEM. In particular, the mesh with 951 elements was enough to produce an acceptable approximated solution for both methods.

Using the mesh with 951 elements, the equivalent stress distribution, under plane strain and perfect plasticity assumption, is shown in Fig. 7a, b, for EbFVM and FEM,

Fig. 4 Flowchart for the return mapping algorithm

I. Check the stress state

$$\sigma_k^j = \sigma_k^c - D^{ep}\Delta\gamma_k^j\sqrt{\frac{3}{2}}\frac{\sigma^d(\sigma_k^j)}{||\sigma^d(\sigma_k^j)||}$$

$$f\left(\sigma_k^j,\gamma_k^j\right) = \sqrt{3J_2(\sigma_k^J)} - Y(\gamma_k^j)$$

If it is in the elastic region, i.e. $f < 0$, then set

$$\sigma_k^{j+1} = \sigma_k^c, \quad \text{and} \quad Y(\gamma_k^{j+1}) = Y(\gamma_k^j)$$

and *EXIT*. Otherwise:

II. Calculate the residuals

$$R_\sigma^j = [D^{ep}]^{-1}\left(\sigma_k^j - \sigma_k^c\right) + \Delta\gamma_k^j\sqrt{\frac{3}{2}}\frac{\sigma^d(\sigma_k^j)}{||\sigma^d(\sigma_k^j)||}$$

$$R_\gamma^j = \sqrt{3J_2\left(\sigma_k^j\right)} - Y(\Delta\gamma_k^j)$$

III. Calculate the Jacobian matrix

$$J = \begin{bmatrix} \dfrac{\partial R_\sigma}{\partial \sigma} & \dfrac{\partial R_\sigma}{\partial \gamma} \\ \dfrac{\partial R_\gamma}{\partial \sigma} & \dfrac{\partial R_\gamma}{\partial \gamma} \end{bmatrix}$$

IV. Evaluate the new variables

$$\begin{bmatrix} \delta\sigma_k^{j+1} \\ \delta\gamma_k^{j+1} \end{bmatrix} = -[J]^{-1}\begin{bmatrix} R_\sigma^j \\ R_\gamma^j \end{bmatrix}$$

V. Update the variables

$$\sigma_k^{j+1} = \sigma_k^j + \delta\sigma_k^{j+1}$$

$$\gamma_k^{j+1} = \gamma_k^j + \delta\gamma_k^{j+1}$$

VI. Check the convergence criteria, i.e. $||R_\sigma^{j+1}||$ and $||R_\gamma^{j+1}|| < \epsilon_{tol}$.

If it is satisfied, then set: $\sigma_k^{n+1} = \sigma_k^{j+1}$ and $D^{ep} := D_{11}$, and *EXIT*.

Otherwise, *GO TO* IV.

respectively. Similar analyses are performed, for linear plasticity, which is presented in Fig. 8. As an additional verification, the von Mises stress state along the minimum section of the plate obtained by EbFVM and FEM is compared in Fig. 9. In order to verify the convergence rate at the global level, the Newton–Raphson convergence for perfect and linear plasticity is shown in Fig. 10.

It is important to acknowledge that, as we would expect, the numerical results of EbFVM and FEM were in good agreement, as can be observed in Figs. 6 through 9. Additionally, the convergence rate of the solution with the mesh size showed by EbFVM was analogous to the one achieved by FEM (Fig. 6). Quadric convergence was achieved by the EbFVM at structural level (Fig. 10), which means this approach was able to handle efficiently the proposed nonlinear application.

In order to make a full description of how EbFVM treats the two-dimensional CSM problem, we present the results

Fig. 5 Domain definition. **a** Plate with a circular hole and **b** section of cylinder

(a)   (b)
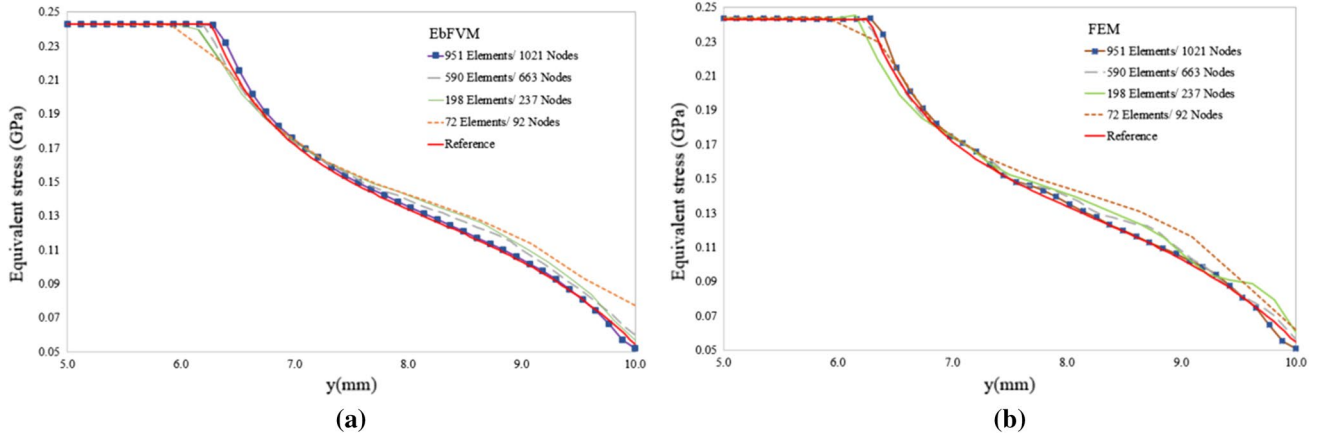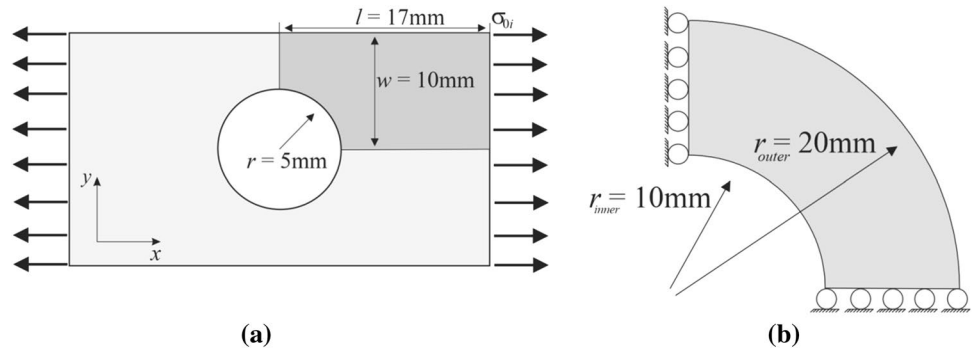
Fig. 6 Equivalent stress using plane strain and linear plasticity assumption. Analyses of mesh size convergence to the exact solution. **a** EbFVM and **b** FEM
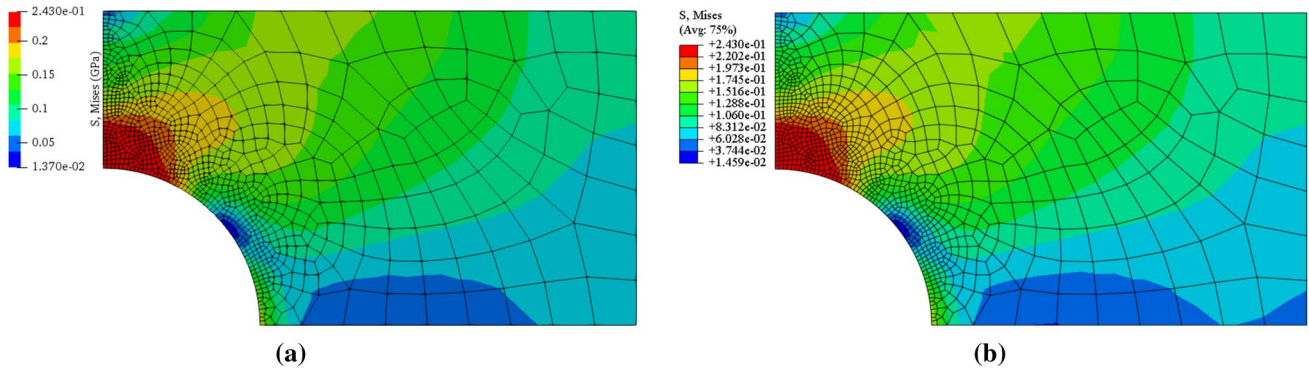
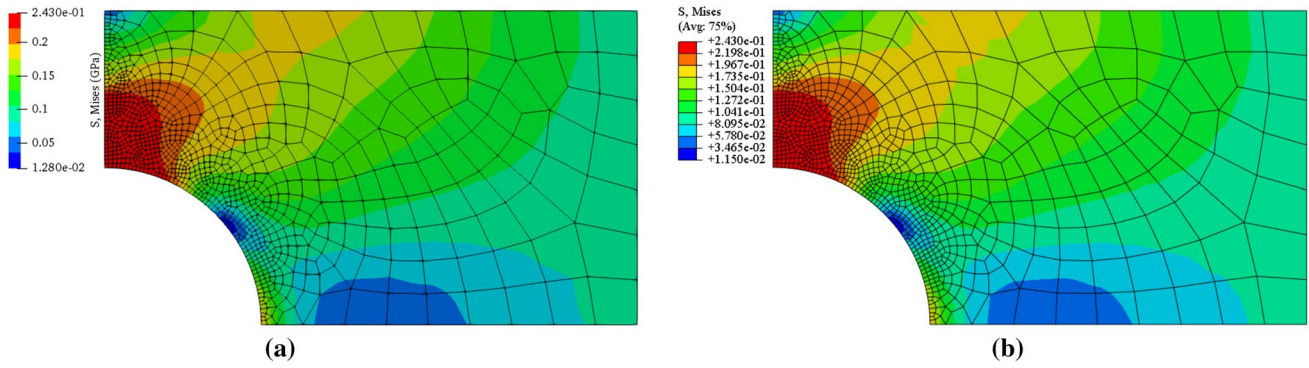**Fig. 7** Equivalent stress field for plane strain and perfect plasticity assumption. **a** EbFVM and **b** FEM

for plane stress in Figs. 11 through 13 using the finest mesh used for the plane strain case. For this case, it was necessary to enforce the normal stress, in z-direction, to be zero at the integration point. Therefore, the equivalent stress state is presented in Fig. 11 for perfect plasticity and in Fig. 12 for linear plasticity. Additionally, the von Mises stress profile along the minimum section of the plate is presented in Fig. 13.

As observed before, similar behavior already commented for plane strain was verified for plane stress. Once again, the results for both approaches are in good agreement with each other and with the reference solution, for perfect and linear plasticity. As for the Newton–Raphson convergence rate, the results, in the plane stress context, for both perfect linear and perfect plasticity are shown in Fig. 14. From this numerical information, it is possible
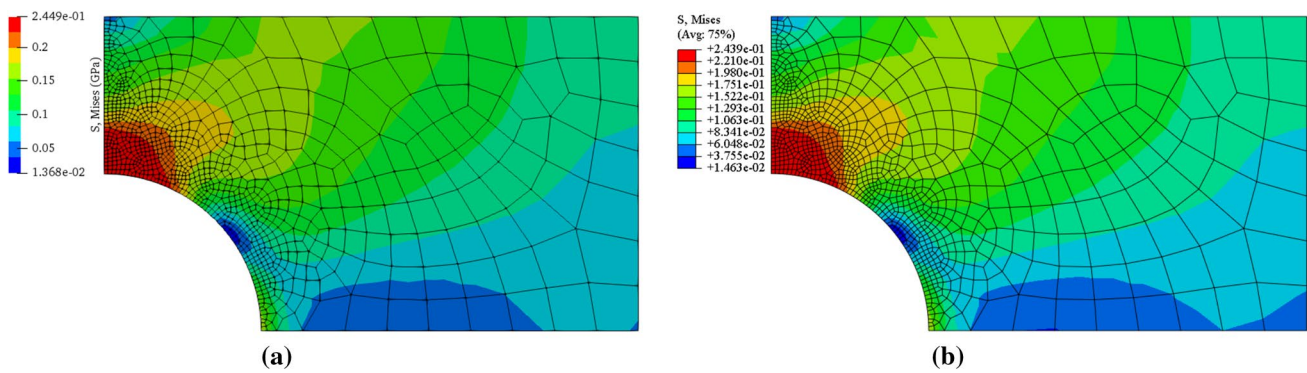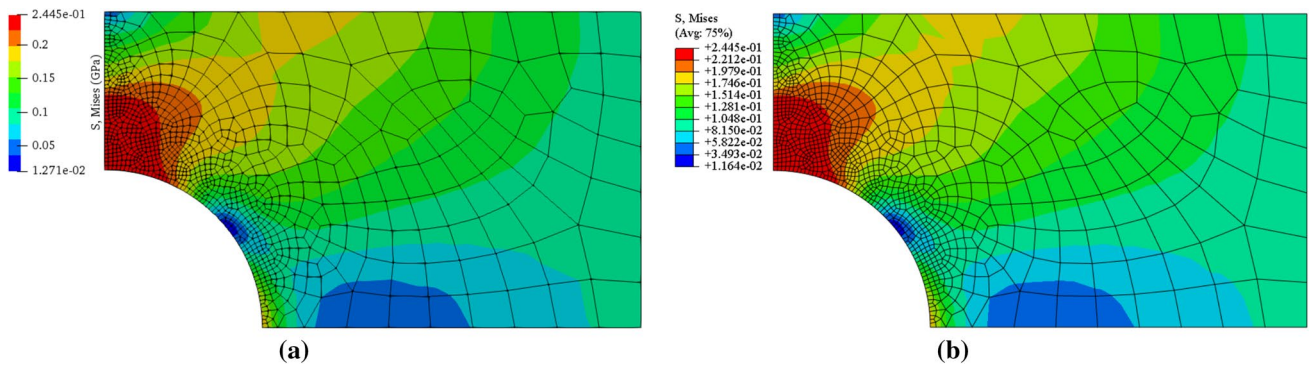
Fig. 8 Equivalent stress field for plane strain and linear plasticity assumption. **a** EbFVM and **b** FEM
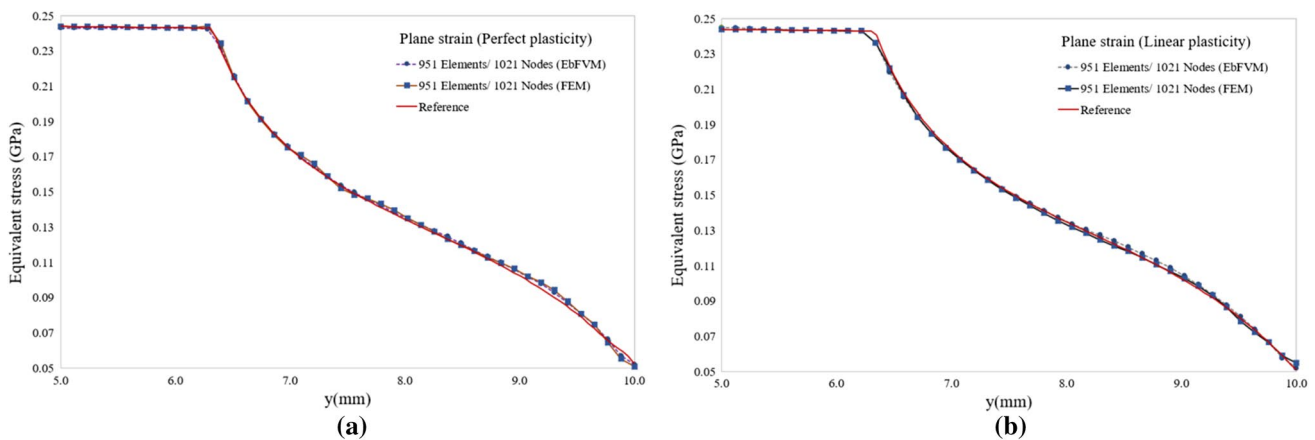
Fig. 9 Plane strain. Comparative equivalent stress between EbFVM and FEM. **a** Perfect plasticity and **b** linear plasticity
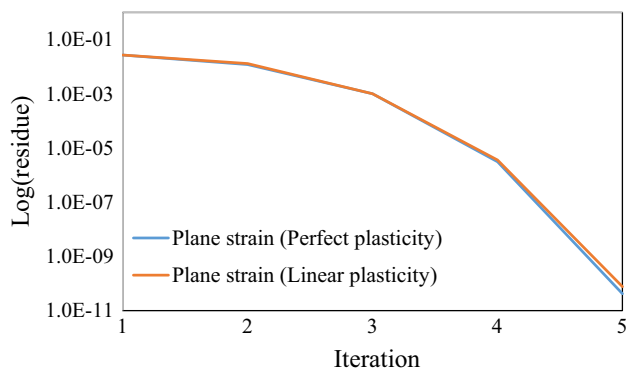
Fig. 10 Plane strain. Residue versus iterations for the last equilibrium increment for perfect and linear plasticity

to verify that five Newton iterations for both mechanics problems were more than enough to obtain a converged solution, in the last load increment. Additionally, we are able to observe quadric convergence for linear and perfect plasticity.

5.2 Thermal expansion

We now investigated the nonlinear problem shown in Fig. 5b, taking into account the thermal expansion. In order to numerically analyze the plasticity loads due to the thermal expansion, we solve separately the energy and the mechanical equations. For solving the energy equation, we applied the following boundary conditions: prescribed temperatures at the inner radius $T_{inner} = 300$ °C and at the outer radius $T_{outer} = 0$ °C, and adiabatic condition at the symmetry regions. After the energy equation was solved, we use the temperature field as input to solve the mechanical problem. In order to avoid rotation and translation of the domain shown in Fig. 5b, we apply Dirichlet boundary condition (∂S_u) fixing the displacement at the symmetrical surfaces.

In order to compare the numerical solution of the EbFVM and FEM, we use the equivalent stress evaluated at the cross section of the domain, which correspond to the *y-axis* and $x = 0$. The solution of both numerical approaches for perfect and linear plasticity for a grid with 800 elements along with the reference solutions for FEM and EbFVM is presented

Fig. 11 Equivalent stress field for plane stress and perfect plasticity assumption. **a** EbFVM and **b** FEM

Fig. 12 Equivalent stress field for plane stress and linear plasticity assumption. **a** EbFVM and **b** FEM
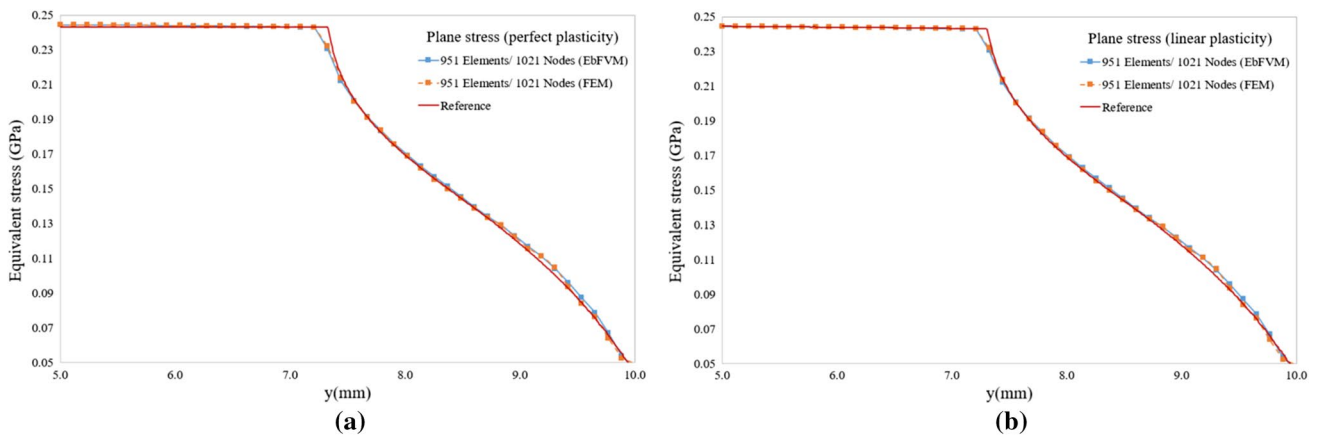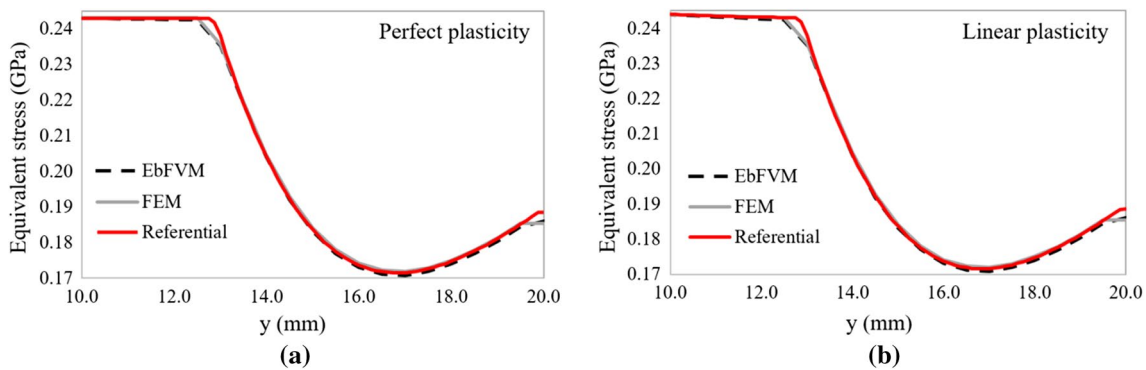

Fig. 13 Plane stress. Comparative equivalent stress between EbFVM and FEM. **a** Perfect plasticity and **b** linear plasticity

in Fig. 15 for plane strain. Unlike the mechanical expansion problems described in Sect. 5.1, we applied only one mesh with 800 elements.

From Fig. 15, we can once again verify that both numerical approaches are in good agreement with each other, and the results are also close to the reference solution. This can

be verified in Figs. 16 and 17 that present the equivalent stress field using both numerical approaches with perfect and linear plasticity for plane strain, respectively.

Our last numerical experiment is devoted to the application of the thermal expansion using plane stress. As was made for plane strain, we have the comparative study
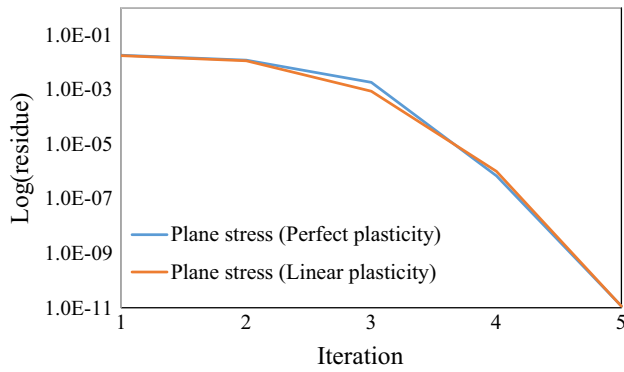
Fig. 14 Plane stress. Residue versus iterations for the last equilibrium increment for perfect and linear plasticity

of equivalent stress profile along the cross section of the domain, as can be observed in Fig. 18 for a grid with 800 elements. Figures 19 and 20 present the von Mises

equivalent stress field for perfect and linear plasticity using plane stress, respectively. Once more, we can verify that the results of EbFVM are in good agreement with the ones obtained with the FEM.

6 Conclusions

In this work, we present the application of the EbFVM to nonlinear material problems. In particular, we numerically analyze the elastic–plastic rate-independent behavior of an isotropic material subject to mechanical and thermal expansions, using plane strain and plane stress assumptions. Additionally, the numerical results are compared with the FEM, in order to analyze if the EbFVM approach could handle these problems in an efficient and accurate way as the FEM does.

The numerical approach using EbFVM was implemented using a Newton–Raphson procedure and PETSc solver

Fig. 15 Thermal plane strain. Comparative equivalent stress between EbFVM and FEM. **a** Perfect plasticity and **b** linear plasticity
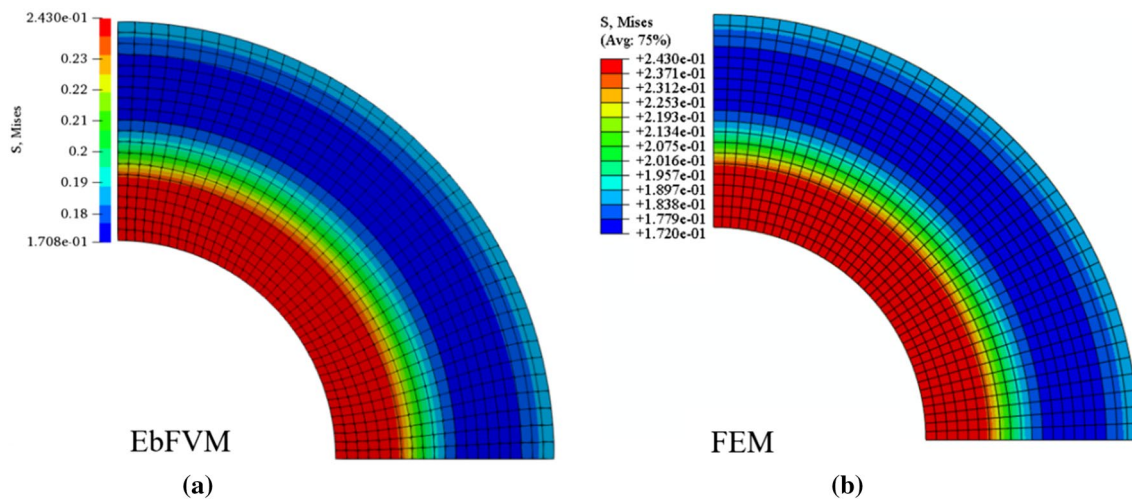
Fig. 16 Plane strain. The von Mises distribution for perfect plasticity. **a** Using EbFVM and **b** using FEM
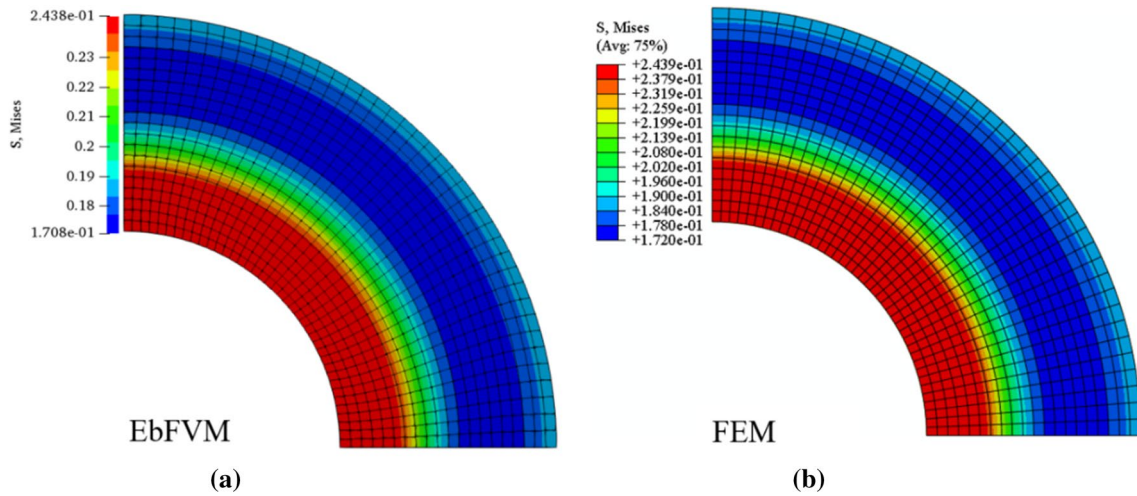
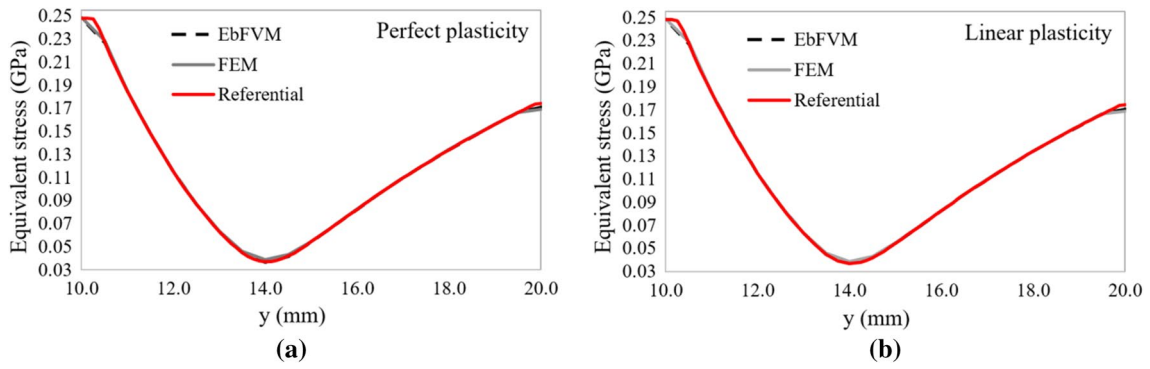**Fig. 17** Plane strain. The von Mises distribution for linear plasticity. **a** Using EbFVM and **b** using FEM

Fig. 18 Thermal plane stress. Comparative equivalent stress between EbFVM and FEM. **a** Perfect plasticity and **b** linear plasticity
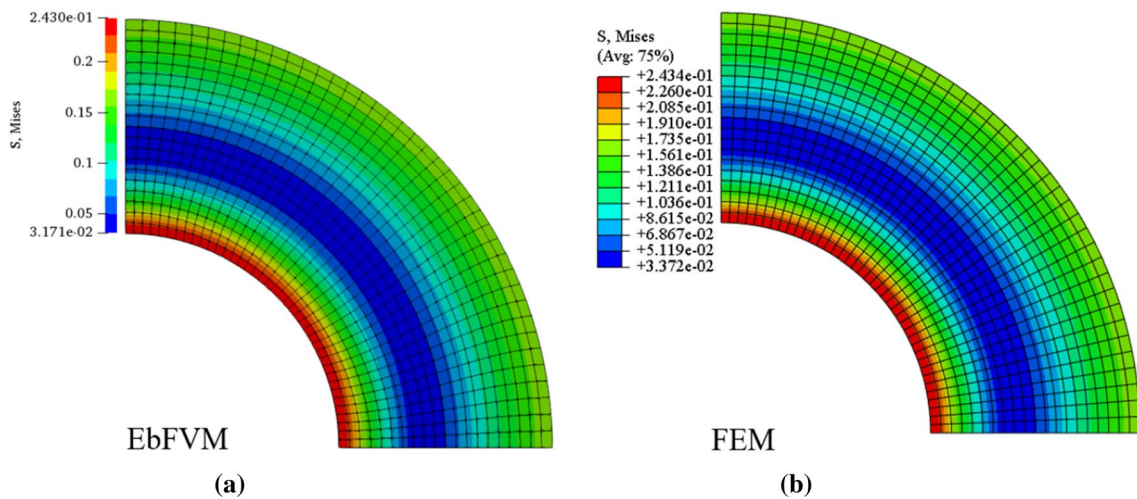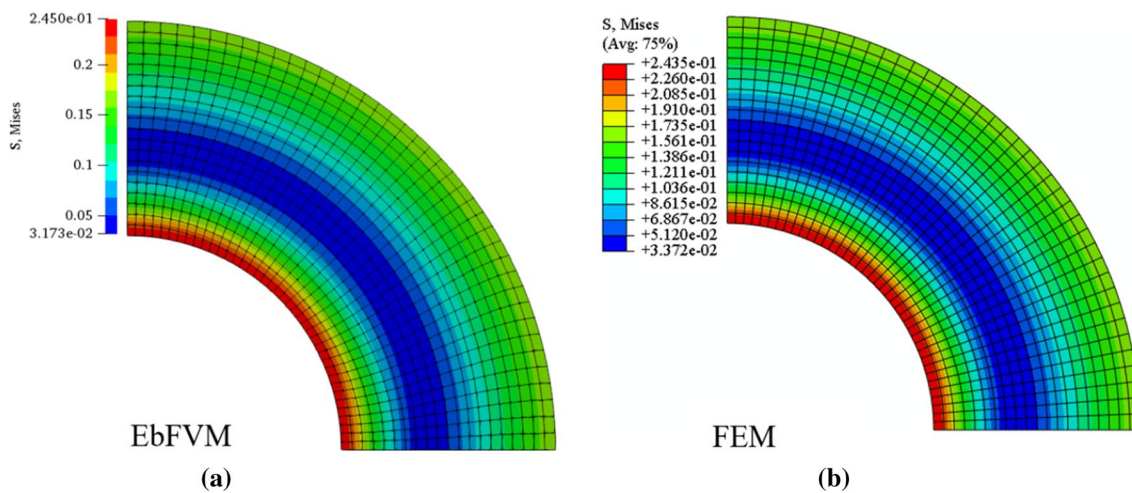

Fig. 19 Plane stress. The von Mises distribution for perfect plasticity. **a** Using EbFVM and **b** using FEM

Fig. 20 Plane stress. The von Mises distribution for linear plasticity. **a** Using EbFVM and **b** using FEM

library. It is remarkable that, throughout the results, the EbFVM provides stable and accurate solution as good as the FEM independently of the load source or the geometrical shape of the domain. The convergence rate of the solution with the mesh size for both EbFVM and FEM was also investigated. From the numerical results, we verified that the convergence rate of both numerical approaches was similar.

The results encourage the development of the EbFVM in fields that FEM is dominant, such as solid mechanics analysis. While EbFVM has attractive characteristics of being conservative at the discrete level, the same in general is not followed by the FEM approach.

References

1. Voller VR (2000) Basic control volume finite element methods for fluids and solids, vol 1. World Scientific, Singapore
2. Zienkiewicz O, Taylor R (2000) The finite element method: solid mechanics, vol 2, 5th edn. Butterworth-Heinemann, Oxford
3. Demirdžić I, Martinović D (1993) Finite volume method for thermo-elastoplastic stress analysis. Comput Methods Appl Mech Eng 109(3–4):331–334. https://doi.org/10.1016/0045-7825(93)90085-C
4. Maliska C (2004) Heat transfer and computational fluid mechanics. LTC, Florianópolis **(in Portuguese)**
5. Taylor G, Bailey C, Cross M (2003) A vertex-based finite volume method applied to non-linear material problems in computational solid mechanics. Int J Numer Methods Eng 56(4):507–529. https://doi.org/10.1002/nme.574
6. Taylor G, Bailey C, Cross M (1995) Solution of the elastic/visco-plastic constitutive equations: a finite volume approach. Appl Math Model 19(12):746–760. https://doi.org/10.1016/0307-904X(95).455.00093-Y
7. Zienkiewick O, Taylor R (1989) The finite element method: basic formulation and linear problems, vol 1. McGraw-Hill Book Company, Maidenhead
8. Bilbao S, Hamilton B (2017) Wave-based room acoustics simulation: explicit/implicit finite volume modeling of viscothermal losses and frequency-dependent boundaries. J Audio Eng Soc 65(1/2):78–89. https://doi.org/10.17743/jaes.2016.0057
9. Slone A, Bailey C, Cross M (2003) Dynamic solid mechanics using finite volume methods. Appl Math Model 27(2):69–87. https://doi.org/10.1016/S0307-904X(02)00060-4
10. Zhang B, Xu C-L, Wang S-M (2017) Generalized source finite volume method for radiative transfer equation in participating media. J Quant Spectrosc Radiat Transf 189:189–197. https://doi.org/10.1016/j.jqsrt.2016.11.025
11. Fernandes BRB, Marcondes F, Sepehrnoori K (2013) Investigation of several interpolation functions for unstructured meshes in conjunction with compositional reservoir simulation. Numer Heat Transf Part A Appl 64(12):974–993. https://doi.org/10.1080/10407782.2013.812006
12. Patankar SV (1980) Numerical heat transfer and fluid flow: computational methods in mechanics and thermal science, vol 1. CRC Press, Boca Raton
13. Baliga B, Patankar S (1980) A new finite-element formulation for convection diffusion problems. Numer Heat Transf 3(4):393–409. https://doi.org/10.1080/01495728008961767
14. Filippini G, Maliska C, Vaz M (2014) A physical perspective of the element-based finite volume method and FEM-Galerkin methods within the framework of the space of finite elements. Int J Numer Meth Eng 98(1):24–43. https://doi.org/10.1002/nme.4618
15. Wheel M (1996) A geometrically versatile finite volume formulation for plane elastostatic stress analysis. J Strain Anal Eng Design 31(2):111–116
16. Woodward CS, Dawson CN (2000) Analysis of expanded mixed finite element methods for a nonlinear parabolic equation modeling flow into variably saturated porous media. SIAM J Numer Anal 37(3):701–724
17. Forsyth PA, Kropinski M (1997) Monotonicity considerations for saturatedunsaturated subsurface flow. SIAM J Sci Comput 18(5):1328–1354

18. Bause M, Knabner P (2004) Computation of variably saturated subsurface flow by adaptive mixed hybrid finite element methods. Adv Water Resour 27(6):565–581

19. Srivastava R, Yeh T-CJ (1992) A three-dimensional numerical model for water flow and transport of chemically reactive solute through porous media under variably saturated conditions. Adv Water Resour 15(5):275–287

20. Jasak H, Weller H (2000) Application of the finite volume method and unstructured meshes to linear elasticity. Int J Numer Meth Eng 48(2):267–287. https://doi.org/10.1002/(SICI)1097-0207(20000520)48:2%3c267:AID-NME884%3e3.0.CO2-Q

21. Fallah N, Bailey C, Cross M, Taylor G (2000) Comparison of finite element and finite volume methods application in geometrically nonlinear stress analysis. Appl Math Model 24(7):439–455. https://doi.org/10.1016/S0307-904X(99)00047-5

22. Moczo P, Robertsson JO, Eisner L (2007) The finite-difference time-domain method for modeling of seismic wave propagation. Adv Geophys 48:421–516

23. Verzicco R, Orlandi P (1996) A finite-difference scheme for three-dimensional incompressible flows in cylindrical coordinates. J Comput Phys 123(2):402–414

24. Ryskin G, Leal L (1984) Numerical solution of free-boundary problems in fluid mechanics. Part 1. The finite-difference technique. J Fluid Mech 148:1–17

25. Suliman R, Oxtoby OF, Malan A, Kok S (2014) An enhanced finite volume method to model 2d linear elastic structures. Appl Math Model 38(7):2265–2279

26. Marcondes F, Sepehrnoori K (2010) An element-based finite-volume method approach for heterogeneous and anisotropic compositional reservoir simulation. J Petrol Sci Eng 73(1):99–106. https://doi.org/10.1016/j.petrol.2010.05.011

27. Winslow AM (1966) Numerical solution of the quasilinear poisson equation in a nonuniform triangle mesh. J Comput Phys 1(2):149–172. https://doi.org/10.1016/0021-9991(66)90001-5

28. Schneider G, Zedan M (1983) Control-volume-based finite element formulation of the heat conduction equation. Spacecr Therm Control Design Oper Prog Astronaut Aeronaut 86:305–327

29. Fryer YD, Bailey C, Cross M, Lai C-H (1991) A control volume procedure for solving the elastic stress-strain equations on an unstructured mesh. Appl Math Model 15(11–12):639–645. https://doi.org/10.1016/S0307-904X(09)81010-X

30. Bailey C, Cross M (1995) A finite volume procedure to solve elastic solid mechanics problems in three dimensions on an unstructured mesh. Int J Numer Methods Eng 38(10):1757–1776. https://doi.org/10.1002/nme.1620381010

31. Idelsohn SR, Oñate E (1994) Finite volumes and finite elements: two good friends. Int J Numer Methods Eng 37(19):3323–3341. https://doi.org/10.1002/nme.1620371908

32. Vaz M, Muñoz-Rojas PA, Filippini G (2009) On the accuracy of nodal stress computation in plane elasticity using finite volumes and finite elements. Comput Struct 87(17):1044–1057. https://doi.org/10.1016/j.compstruc.2009.05.007

33. Demirdžić I, Muzaferija S (1994) Finite volume method for stress analysis in complex domains. Int J Numer Methods Eng 37(21):3751–3766. https://doi.org/10.1002/nme.1620372110

34. de Souza Neto EA, Peric D, Owen DR (2011) Computational methods for plasticity: theory and applications. Wiley, New York

35. Simo JC, Hughes TJ (2006) Computational inelasticity, vol 7. Springer, Berlin

36. Crisfield MA, Remmers JJ, Verhoosel CV et al (2012) Nonlinear finite element analysis of solids and structures. Wiley, New York

37. Kim N-H (2014) Introduction to nonlinear finite element analysis. Springer, Berlin

38. Logan D (2002) First course in finite element analysis. Brooks/Cole, Boston